Dynamic response of wrought and additively manufactured nickel-based alloys to high velocity impacts of laser-launched flyers

E. Barraud, T. de Rességuier, J. Baillargeat, S. Hemery, Jonathan Cormier

Dynamic response of wrought and additively manufactured Nickel-based alloys to high velocity impacts of laser-launched flyers

E. Barraud*, T. de Rességuier, J. Baillargeat, S. Hemery, J. Cormier

Institut Pprime, UPR 3346, CNRS, ISAE-ENSMA, Université de Poitiers, Futuroscope Cedex, FRANCE

** Corresponding author. E-mail address: etienne.barraud@ensma.fr (E. Barraud)*

ABSTRACT

Although Nickel-based superalloys are widely used in the industry, their response to shock loading is still rarely investigated. Here, the impacts of laser-launched flyers were used to study the dynamic behavior of Rene 65 superalloy under shock pressures of about 10 GPa at very high strain rates of about 10^6 s^{-1}. Three types of samples, wrought or additively manufactured (laser powder bed fusion) and subjected to different heat treatment conditions, were investigated. These experiments allowed the measurement of the Hugoniot elastic limit (compressive yield strength) and the spall (tensile) strength, both in upper ranges compared with most common metals. Post-recovery analyses involving various techniques provided insight into dynamic failure, with a combination of transgranular ductile fracture and intergranular cracks with preferential nucleation sites, strongly dependent on the different microstructures related to fabrication routes and thermal treatments.

1. INTRODUCTION

Due to their unique combination of excellent corrosion, oxidation and mechanical properties at high temperatures, Ni-based superalloys are widely used in various fields such as aero-engines, gas turbines for power generation, petrochemistry or even Formula one turbochargers. Nowadays, they account for nearly 50% of the mass of an aircraft engine. Despite extensive documentation on their thermomechanical behavior under quasi-static loading[1–3] and fatigue life[4,5], scarce data can be found yet on their behavior under dynamic loading[6,7], in particular at very high deformation rates[8]. Some have been subjected to peening treatments, including laser shock peening, to improve their fatigue properties[9,10], but the systematic investigation of their response to higher shock loading is still a largely open field. It is also a practical engineering need since aircraft components can be subjected to severe dynamic solicitations, e.g. in cases of a bird strike, high velocity impacts of ice, gravel or dust particles, or blade failure within the engine.

On the other hand, the rapid growth of additive manufacturing (AM) processes in the industry spreads to the aeronautical sector, which must remain competitive in a sustainable environment. Indeed, these processes offer numerous and multi-faceted opportunities: technological, since engines include complex components, economic, with fewer tools, and ecological, by lightening the structures and reducing the buy-to-fly ratio. Many reports summarize the challenges of AM[11–13], some more specific to the aerospace sector[14] and Ni-superalloys[15,16]. Fewer papers can be found on the effects of AM on the high-strain rate behavior of materials thus produced[17-24]. For example, recent work on a light Al alloy obtained by selective laser melting have provided key information on its dynamic compressive yield strength and tensile strength, as well as evidence of the strong influence of the AM-inherited mesostructure (so-called melt pools) on crack initiation and propagation[20,22].

In this paper, we investigate the shock behavior of a Rene 65 Ni-based superalloy[1,4,25,26]. Its composition (Table I) rich in refractory elements comes with excellent mechanical properties at high temperatures so that it is used in the most recent generation of aero-engines. Specimens obtained from an AM

process, namely Laser Powder Bed Fusion (LPBF), are compared with wrought samples, and two different heat treatment conditions are considered. This leads to substantially different microstructures. Samples are subjected to planar shock loading upon high velocity impact of thin Al plates accelerated by a high intensity laser pulse. Time-resolved velocity measurements provide the Hugoniot yield strength and spall strength of the alloys. In addition, post-recovery analyses involving a variety of complementary techniques give insights into the processes governing dynamic fracture and their dependence on the initial microstructures.

2. MATERIAL

Rene 65 Ni-based superalloy has recently appeared as an appealing candidate to withstand the extreme temperature gradients involved in AM processes such as laser fusion on powder bed (LPBF) or more specifically direct metal laser melting. Furthermore, heat treatments both below (sub-) and above (super-) the gamma prime (γ') solvus have been shown to affect tensile, fatigue and creep behavior of the alloy[11], with some interest for specific applications. Our experiments were performed on the same materials, produced by LPBF, i.e. laser melting of a powder layer by layer with a build direction referred as Z, followed by hot isostatic pressing to compact the material and remove porosity. Details on the complete process belong to the provider. The same two thermal treatments mentioned above were performed prior to shock loading, subsolvus (annealing at 1080 °C) and supersolvus (annealing at 1120 °C). Finally, cast and wrought Rene 65 obtained from a ring-rolled component, subsolvus heat-treated, was tested for comparison.

The initial microstructures and grain morphologies were characterized using the Electron Back Scattered Diffraction (EBSD) technique. A JEOL™ 6100 scanning electron microscope (SEM) operated at 25 kV equipped with an Hikari EBSD detector and an OIM-EDAX system was used. Step sizes in the 0.25 – 0.40 µm range were applied to properly characterize microstructural features. Specimens were first ground using SiC paper and then polished using diamond suspensions. A final polishing step was applied using a solution of colloidal silica containing 0.04 µm particles. Crystallographic orientation maps shown in Fig. 1 reveal microstructural features consistent with previous observations[11]. The wrought material (Fig. 1a) exhibits a grain size in the 10 µm range, with numerous twins, as well as primary γ' precipitates of about 3 µm-diameter located at grain boundaries, and carbide particles of similar size (which will be shown further in Section 4). Although not displayed for clarity purposes, the texture in this material is weak. In contrast, the AM alloy in the subsolvus treated form (Fig. 1b) presents elongated, columnar grains with dimensions about 100 to 250 µm along the building direction (Z). Such columnar morphology likely results from the vertical thermal gradient during the layer-by-layer AM process, as commonly reported in the literature for superalloys made by LPBF[27–29]. In agreement with classical AM microstructures as well, this is accompanied by a preferential [001] orientation along the build direction, like for all other face-centered-cubic materials. In contrast to the wrought material, this AM microstructure does not show any twin, primary γ' precipitate, nor large carbide particles. Still, grains contain tiny, secondary γ' precipitates in the 100-500 nm range[15]. Finally, supersolvus treated AM specimens (Fig. 1c) display equiaxed grains with a diameter about 80 µm. As observed for the wrought sample, twins are present. In addition, the texture is weak. Besides, X-ray radiographs have shown that these alloys do not present any pore (larger than the 5 µm spatial resolution).

Rods of diameters between 12 and 16 mm were extracted from the bulk, along the Z direction in the AM alloys, then sectioned into thin plates by electrical discharge machining. Plate thickness was reduced to about 400 µm by mechanical polishing with 500 grit silicon carbide paper. The final samples consist of thin disks with a mean thickness of 404 µm and a standard deviation of 19 µm (about 5 %).

Shock behavior of materials is largely dependent on density and sound speed. The density ρ_0 of the different materials was determined by mass and volume measurements, and both longitudinal (C_l) and

transverse (C_t) elastic wave velocities were measured ultrasonically in the material rods (as stated earlier, the AM rods are parallel to the Z direction). The bulk sound speed C_b was then calculated as

$$C_b = \sqrt{C_l^2 - \frac{4}{3}C_t^2} \quad (1)$$

The resulting values are plotted in Fig. 2 for the different manufacturing routes and heat treatments. The small discrepancies are very likely due to natural scatter of such measurements rather than to significant, physical differences between the three sample types. Unfortunately the natural scatter could not be quantified because only one rod of each kind could be tested.

3. EXPERIMENTAL TECHNIQUES

The experiments were performed at Institut Pprime. High pressure shock loading of the Ni-alloy targets was achieved through planar impact of thin Al foils accelerated by pulsed laser ablation in confined geometry. This technique has been widely used in the past to investigate shock initiation of condensed explosives[30,31] and more generally the dynamic behavior of condensed matter[32–35].

3.1 Laser-driven acceleration of thin Al flyers

A laser pulse of 1053 nm wavelength, about 20 J energy and about 35 ns duration at half maximum is focused onto a 3.5 mm-diameter spot in the surface of a 150 µm-thick Al foil. At each shot, pulse duration is recorded with a high speed photodiode and energy is inferred from a small, calibrated portion of light transmitted through a mirror and measured with a calorimeter. The resulting intensity is about 6 GW/cm². A thin (µm-order) absorbing layer of Al is ablated into a plasma cloud, which expands towards the laser source and drives by reaction a compressive pulse into the solid foil. In order to enhance both the amplitude and duration of this compression, a water layer (a few mm-thick, transparent to the laser light) is pooled on top of the Al surface before the shot (Fig. 3a). It confines the plasma expansion, so that the pressure load applied on this surface is higher and longer than under direct laser-matter interaction in vacuum[36,37]. However, the maximum laser intensity is then bounded below an ionization threshold above which the confining medium absorbs the laser energy (so-called laser breakdown). With similar laser parameters (i.e. pulses of 1.06 µm-wavelength and 25-30 ns duration in water-confined geometry), this threshold was reported to be about 10 GW/cm² [37]. Although this is significantly higher than the mean intensity in our experiments, partial laser breakdown occurred in a few of our shots, probably because of a non-homogeneous energy distribution within the laser beam leading to hot spots in the irradiated surface. As will be discussed further, such shots resulted in flyer velocities lower than expected.

Time-resolved velocity measurements were performed with a Velocity Interferometer System for Any Reflector (VISAR)[38], in a push-pull configuration[39]. The free surface of the Al foil, opposite to the irradiated spot is illuminated by a continuous laser of 532 nm-wavelength (Fig. 3a). The light reflected by this moving surface is sent to the interferometer where Doppler-based interference patterns are created and recorded by photomultipliers with a time resolution of about 1 ns. The fringe factor was chosen as 843 m/s, greater than the expected velocity jumps to ensure that no fringe would be lost upon shock breakout. A polycarbonate shield was inserted below the foil to protect the VISAR lens (Fig. 3a).

A typical velocity record is shown in Fig. 3b. When the laser-driven shock breaks out at the free surface of the foil, this surface is accelerated to a peak velocity of 486 m/s. According to a classical assumption fully relevant at moderate pressure, this value is twice the particle velocity U_p induced behind the shock front. Using the conservation equation $P = \rho_{0A} U_s U_p$, where $\rho_{0A} = 2.784$ g/cm^3 is the initial density of Al, $U_p = 243$ m/s, and $U_s = C_{0A} + S_A U_p$ is the shock velocity with $C_{0A} = 5209$ m/s and $S_A = 1.338$ for Al [40], shock pressure P is evaluated at 3.7 GPa. This is in very good agreement with data reported for similar laser shocks in water-confined geometry[37]. Thereafter, the record shows velocity oscillations

corresponding to wave reverberation between the irradiated surface, where the plasma still exerts a decreasing pressure producing successive reloading waves, and the probed free surface. Thus, the period of these oscillations, about 42 ns, is twice the transit time of a pressure wave (travelling approximately at the sound velocity C_{0A} in Al) across the 150 µm-thick foil (back and forth). Finally, within about 600 ns, the velocity reaches a plateau at about 1000 m/s, fully consistent with ranges reported in the past[35].

3.2 Impact loading of Ni-based alloys

The laser-launched Al foils were used as flyers to generate impact loading of the Ni-alloy samples. The corresponding setup is described schematically in Fig. 4. As detailed in the previous subsection, the Al foil is accelerated by laser irradiation in water confined geometry, it travels across a gap delimited by a 250 µm-thick ring of inner diameter 8 mm, before impacting the Ni-alloy target. Lateral dimensions (laser spot diameter and ring diameter) are much larger than the overall thickness of the assembly (foil + ring + target). Therefore, conditions of one-dimensional (1D) strain following planar impact can be expected in the central region of the sample if laser energy distribution is assumed to be uniform over the irradiated spot. The impact velocity can be calculated by integrating the free surface velocity of the foil until the resulting distance (blue area in Fig. 3b) matches the 250 µm-width of the gap. This gap should be large enough to let the flyer reach the velocity plateau but not much larger to limit foil deformations which would degrade impact planarity. Hence, the flyer corresponding to Fig. 3b would impact the target after about 430 ns at a 900 m/s impact velocity. The same VISAR setup as in Fig. 3a allows measuring the velocity of the (bottom) free surface of the Ni-alloy target, opposite to the impacted surface (Fig. 4).

To evaluate the shock pressure induced in the target, a simple hydrodynamic description accounting for impedance mismatch between the Al flyer and the Ni-alloy can be performed (Fig. 5). Using the equations and parameters recalled in subsection 3.1, the shock adiabat of Al can be plotted in a P-U_p diagram (blue solid line). Because the relationship between U_s and U_p in the Rene 65 Ni-based alloy is essentially unknown yet, shock velocity can be approximated by bulk sound velocity (using the so-called acoustic approximation). The target adiabat is then plotted as a straight line (red line) of slope $\rho_0 C_b$ (values in Fig. 2). Ambient pressure is neglected. Just before impact, the Al flyer is at $P \approx 0$ and U_p = 900 m/s (state 1 in Fig. 5). Upon impact, both the Al flyer and the alloy target are shocked to state 2, so that shock pressure can be quantified to 10.5 GPa (Fig. 5). Finally, when this impact-induced shock wave will reflect from the target free surface, the Ni-alloy will be released down to state 3, so that a ~540 m/s jump in the free surface velocity is expected then.

4. RESULTS AND DISCUSSION

4.1 Time-resolved velocity measurements

A typical VISAR record of the target free surface velocity is plotted in Fig. 6.

The first wave to emerge at the free surface is called the elastic precursor. It propagates at the elastic sound velocity C_l and produces an elastic compression up to the Hugoniot Elastic Limit (HEL), associated with a first jump to a free surface velocity of 100 m/s in the record, equal to twice the particle velocity U_{HEL}. The dynamic yield strength is then derived as

$$\sigma_{HEL} = \rho_0 C_l U_{HEL} \quad (2)$$

This elastic wave is followed by a plastic compression wave, accelerating the free surface to a peak velocity of 560 m/s, in very good agreement with the 540 m/s value expected from the simple hydrodynamic analysis in Fig. 5 (Section 3.2). Next, an unloading wave generated by the reflection of the shock front at the back surface of the Al flyer (upper surface in Fig. 4) reaches the target free surface, producing a deceleration called the velocity pullback. Within the sample, the interaction of this incident unloading wave with the rarefaction wave produced upon reflection of the shock front from the bottom free surface creates tensile stresses. They produce damage if they exceed the dynamic tensile strength (or spall strength) of the material[41,42]. Thus, at about 740 ns, the deceleration is interrupted by the arrival of a recompression wave due to stress relaxation upon crack opening (i.e. spall fracture) inside the target. Finally, the record presents velocity oscillations associated with wave reverberation across the spalled layer, i.e. between the internal spall plane and the probed free surface. Considering the bulk sound velocity C_b of about 4700 m/s (Fig. 2), the ~45 ns period of these oscillations indicates a spall thickness of about 100 µm.

Theoretical analyses of wave dynamics during the spalling process provide simple relations between the amplitude of the velocity pullback ΔU_{FS} (see Fig. 6) and the spall strength[42,43]. In an elastic-plastic medium, the spall strength can be evaluated as

$$\sigma_{sp} = \rho_0 C_b \frac{1}{1+\frac{C_b}{C_l}} \Delta U_{FS} \quad (3)$$

Besides, an estimate of the strain rate is given by

$$\dot{\varepsilon} = \frac{1}{2C_b} \frac{\Delta U_{FS}}{\Delta t} \quad (4)$$

where Δt is the duration of the free surface deceleration in the record (see Fig. 6).

In the experiments reported here, the peak free surface velocity was found to vary between 325 m/s and 665 m/s (with most values around 530 m/s). This scatter is attributed to shot-to-shot variations of impact velocities, not clearly correlated with the measured laser parameters (energy and pulse duration) nor with the type of Ni-alloy target. Instead, such variations probably result from irregular deformation of the Al foil during its flight, leading to imperfect planarity and defective parallelism at impact. They could also come from partial laser breakdown in the confining water, as mentioned in Section 3.1, likely due to non-homogeneous energy distribution in the laser beam. Still, these variations do not affect the measured strength values, which is consistent with the literature (i.e. generally weak influence of shock pressure on both the yield strength and the spall strength). The measured values of the Hugoniot elastic limit σ_{HEL} (Eq. 2) and spall strength σ_{sp} (Eq. 3) are presented in Fig. 7 and Fig. 8, respectively. The strain rate inferred from Eq. 4 is about 10^6 s^{-1} in all shots. Mean values are indicated in bold numbers for the three tested materials. Error bars, corresponding to the standard deviation around the mean value, reflect the scattering between the shots. Within such error bars, no significant difference can be asserted between the three different types of specimens. Still, an overall trend suggests slightly higher spall strength in the AM materials, both subsolvus and supersolvus, than in the wrought alloy, which would be consistent with larger grain sizes (see Fig. 1) as will be discussed in more details next. Zaretsky et al.[8] reported analogous data on two other Ni-based alloys, Inconel 738 LC and PWA 1483, subjected to plate impacts at strain rates in the 10^5 s^{-1} range. These data are compared with our results in Table II. The higher spall strength in our experiments can be partially attributed to the higher strain rate, as well as a higher resistance of Rene 65[15,44–46]. This very high spall strength of Rene 65, about 5 GPa, can be compared with that of high strength metals such as Ti alloys (between 3.7 and 5 GPa) or Ta (about 4.5 GPa)[42].

4.2 Post-recovery observations

One advantage of the shock loading technique considered here over more conventional plate impact experiments involving gas guns or explosive-driven projectiles is the very easy recovery of the shocked specimens, which remain attached to the sample holder after the shot. This allows detailed post-test observations which are illustrated in this subsection.

Preliminary examination of some recovered Ni-alloy targets was performed in X-ray microtomography, with a spatial resolution of 5 µm/voxel. It revealed extensive spall damage inside the bulk, forming a well-defined spall plane beneath the free surface (Fig. 9), consistent with the velocity records (see previous subsection) and confirming to some extent the correct planarity of impact loading. Different damage stages were observed, from barely open fracture at the spall plane to full separation of the spalled layer, which confirms some variations in impact velocities as discussed above. Microtomography will also be used to investigate possible anisotropic effects related to initial microstructures (see Fig. 1b), taking advantage of the 3D scan to extract sections with various orientations, but this work is currently in progress.

An overall view of a cross section in a shock-recovered wrought specimen is presented in Fig. 10a. It shows a main crack roughly parallel to the free surface. Dimples left by the nucleation, growth and coalescence of spherical voids testify of ductile damage. The ~100 µm thickness of the spalled layer is fully consistent with that inferred from the final oscillations in the velocity record (subsection 4.1). Higher magnification micrographs in back-scattered electron imaging (Fig. 10b, 10c) strongly suggest that voids nucleated preferentially at primary γ' (dark grey spots) and carbide particles (white), both located at grain boundaries, then developed throughout and propagated from one of these inclusions to the next. Thus, the ductile failure along the spall plane appears to be mainly intergranular, as confirmed by EBSD analyses (Fig. 11).

Crack nucleation at non-metallic inclusions in Ni-based superalloys has already been reported under both static and cycle loads[47–50]. As for preferential crack initiation at the primary γ' particles, a fundamental reason could be that they are in most cases only partially coherent with their surrounding grains. Besides, depending on the forging conditions, they can also be surrounded by a ductile γ-shell depleted of fine strengthening γ' precipitates, as previously reported by Charpagne et al[51–53]. Such a lack of coherence of primary γ'particles interfaces, and a possible very narrow precipitate-free zone in their immediate vicinity, are likely to favour preferred damage development in dynamic conditions.

Post-recovery observations in subsolvus heat treated AM samples are presented in Fig. 12 to 14. Cross sections still show a main crack along a spall plane roughly parallel to the free surface, resulting mainly from ductile failure as demonstrated by the presence of dimples. However, short, smooth cracks and crack branching can also be seen along the perpendicular direction, leading to a "staircase" profile of the macroscopic fracture (Fig. 12a). Closer views show that most of these cracks originate at grain boundaries (Fig. 12b). They also confirm the presence of secondary γ' precipitates (dark grey) mentioned in Section 2, likely too small to play the same role (i.e. sites for void nucleation) as the larger ones in the wrought material.

A few shots produced full ejection of the spalled layer, leaving an open crater in the sample free surface. The bottom of these craters was observed in SEM, for a complementary characterization of the fracture surface morphology. Such micrographs are shown in Fig. 13, for a subsolvus AM specimen. They confirm the statements inferred from the cross sections, i.e. clear evidence of ductile fracture within the spall plane combined with some short cracks normal to this plane, with smooth facets suggesting intergranular fracture.

An EBSD map in a shocked specimen of subsolvus AM Rene 65 is shown in Fig. 14. The direction of shock application matches the Z direction. As already inferred from the micrographs (Fig. 12) and in contrast with the wrought material (i.e. in the absence of large carbides and primary γ' precipitates), voids seem to nucleate predominantly at grain boundaries, then grow and coalesce across the grains width (over comparatively short distances given their aspect ratio and orientation). This results in mainly transgranular, ductile fracture in the spall plane. In addition, a few short cracks are seen to run along some grain boundaries normally to the spall plane, in the Z direction (Fig. 14a). They account for the staircase profile in Fig. 12a and smooth facets in Fig. 13. Overall, because grains are significantly larger than in the wrought samples and because of the absence of primary γ' precipitates and large carbides providing nucleation sites, one might expect a somewhat higher spall strength in the AM material, which would be consistent with the trend suggested in Fig. 8.

Fig. 15 shows typical EBSD maps in a shocked sample of supersolvus heat treated AM Rene 65. Like in the subsolvus case above, voids are seen to nucleate mostly at grain boundaries (see the close-up view in Fig. 15b). Then a combination of mainly transgranular cracks along the spall plane with fewer and shorter intergranular cracks in the normal direction leads to a similar staircase fracture profile. Overall, pre-existing twins (see Fig. 1c) are not found to significantly affect damage and their boundaries do not seem to constitute preferred sites for void nucleation. These observations are fully consistent with the fact that subsolvus and supersolvus AM specimens present similar spall strength values (Fig. 8).

Finally, such EBSD maps did not reveal any additional twins, not beneath the impacted surface where shock compression was intense nor near the edges of this impacted zone where severe shear loading was induced. Thus, shock-induced plastic deformation was probably accommodated mainly through dislocation slip without mechanical twinning.

5. CONCLUSION

High power laser pulses were used to accelerate 150 µm-thick Al flyers up to about 1 km/s velocities. The impact of such flyers allowed studying the dynamic response of both cast and wrought and additively manufactured specimens of Rene 65 Ni-based superalloy to shock compression in the 10 GPa pressure range, for two different heat treatments prior to shock loading. The Hugoniot elastic limit (or dynamic yield strength) and spall strength (or dynamic tensile strength) of these materials were determined at very high strain rates on the order of 10^6 s^{-1}. Within the experimental uncertainties, both values seem almost insensitive to the manufacturing route and thermal treatment. They are both comparable with data reported for pure, high-strength metals commonly used for armoring applications, indicating a very high resistance of the superalloy to shock loading. Since our experimental technique allows easy and direct sample recovery, post-shot observations of the impacted specimens were carried out, using X-ray microtomography, optical microscopy and scanning electron microscopy, including electron back-scattered diffraction. They revealed a dynamic fracture process mainly governed by ductile damage, which was shown, unlike the strength values, to strongly depend on the microstructure, closely related to sample fabrication and processing. Thus, in the wrought material, cracks nucleate preferentially at primary γ' precipitates interfaces or at large carbide particles, then fracture is mainly intergranular. In contrast, in the absence of such ~µm-size inclusions in the AM material, void nucleation occurs mainly at grain boundaries, followed by transgranular growth and propagation along the spall plane, combined with a few additional intergranular cracks in the perpendicular direction. Future work will include additional efforts to identify plastic deformation mechanisms, to be correlated with the manufacturing and processing routes. The anisotropy in the dynamic response of the AM alloys will also be investigated by varying the direction of load application with respect to their building direction.

ACKNOWLEDGMENTS

Authors are grateful to Amélie Caradec and Florence Hamon for their kind help with SEM observations and to David Mellier for running the XCT tomographic characterization. Authors are also grateful to GE Additive, and more specifically to Dr. Andrew Wessman (formerly at GE Additive and now at the University of Arizona in Tucson) for providing almost defect-free AM processed Rene 65 specimens. Safran Aircraft Engines (and more specifically Dr. Thomas Billot) is also acknowledged for providing Rene 65 cast and wrought material. This work was partially funded by Agence de l'innovation de défense, by the French Government program Investissements d'Avenir (EQUIPEX GAP, reference ANR-11-EQPX-0018), by the Contrat de Plan Etat-Région (CPER) Nouvelle-Aquitaine and by the Fonds Européen de Développement Régional (FEDER).

DECLARATION OF INTEREST

All authors certify that they have no affiliations with or involvement in any organization or entity with any financial interest or non-financial interest in the subject matter or materials discussed in this manuscript. The authors have no financial or proprietary interests in any material discussed in this article.

DATA AVAILABILITY STATEMENT

The data that support the findings of this study are available from the corresponding author upon reasonable request.

REFERENCES

[1] J.A. Heaney, M.L. Lasonde, and A.M. Powell, Development of a new cast and wrought alloy (Rene 65) for high temperature disk applications, in *8th International Symposium on Superalloy 718 and Derivatives* (The Minerals, Metals & Materials Society, 2014), p. 11.

[2] R.C. Reed, *The Superalloys: Fundamentals and Applications*, Cambridge University Press (2006).

[3] T.M. Pollock and S. Tin, Nickel-based superalloys for advanced turbine engines: chemistry, microstructure and properties, Journal of Propulsion and Power **22**, 361 (2006).

[4] A. Wessman, A. Laurence, J. Cormier, P. Villechaise, T. Billot, and J.M. Franchet, Thermal stability of cast and wrought alloy Rene 65, in *Proceedings of the 13th International Symposium on Superalloys* (The Minerals, Metals & Materials Society, 2016), pp. 793–800.

[5] A. Pineau and S.D. Antolovich, High temperature fatighe of nickel-base superalloys - A review with special emphasis on deformation modes and oxidation, Engineering Failure Analysis **16**, 2668 (2009).

[6] B. Erice, M.J. Pérez-Martín, and F. Gálvez, An experimental and numerical study of ductile failure under quasi-static and impact loadings of Inconel 718 nickel-base superalloy, International Journal of Impact Engineering **69**, 11 (2014).

[7] J. Wang, W.-G. Guo, Y. Su, P. Zhou, and K. Yuan, Anomalous behaviors of a single-crystal Nickel-base superalloy over a wide range of temperatures and strain rates, Mechanics of Materials **94**, 79 (2016).

[8] E.B. Zaretsky, G.I. Kanel, S.V. Razorenov, and K. Baumung, Impact strength properties of nickel-based refractory superalloys at normal and elevated temperatures, International Journal of Impact Engineering **31**, 41 (2005).

[9] P. Forget, J.L. Strudel, M. Jeandin, J. Lu, and L. Castex, Laser shock surface treatment of Ni-based superalloys, Materials and Manufacturing Processes **5**, 501 (1990).

[10] W. Zhou, X. Ren, Y. Yang, Z. Tong, and L. Chen, Tensile behavior of nickel with gradient microstructure produced by laser shock peening, Materials Science and Engineering: A **771**, 138603 (2020).

[11] W.E. Frazier, Metal Additive Manufacturing: A Review, J. of Mater Eng and Perform **23**, 1917 (2014).

[12] J. Gardan, Additive manufacturing technologies: state of the art and trends, International Journal of Production Research **54**, 3118 (2016).

[13] E.O. Olakanmi, R.F. Cochrane, and K.W. Dalgarno, A review n selective laser sintering/melting (SLS/SLM) of aluminium alloy pawders: Processing, microstructure and properties, Progress in Materials Science **74**, 401 (2015).

[14] B. Blakey-Milner, P. Gradl, G. Snedden, M. Brooks, J. Pitot, E. Lopez, M. Leary, F. Berto, and A. du Plessis, Metal additive manufacturing in aerospace: A review, Materials & Design **209**, 110008 (2021).

[15] A. Wessman, J. Cormier, F. Hamon, K. Rainey, S. Tin, D. Tiparti, and L. Dial, Microstructure and mechanical properties of additively manufactured Rene 65, in *Superalloys 2020: Proceedings of the 14th International Symposium on Superalloys* (Springer International Publishing, Cham, 2020), pp. 961–971.

[16] S. Sanchez, P. Smith, Z. Xu, G. Gaspard, C.J. Hyde, W.W. Wits, I.A. Ashcroft, H. Chen, and A.T. Clare, Powder Bed Fusion of nickel-based superalloys: A review, International Journal of Machine Tools and Manufacture **165**, 103729 (2021).

[17] D.R. Jones, S.J. Fensin, O. Dippo, R.A. Beal, V. Livescu, D.T. MArtinez, C.P. Trujillo, J.N. Florando, M. Kumar, G.T. Gray III, Spall Fracture in additive manufactured Ti-6Al-4V, J. Appl. Phys. **120**, 135902, (2016).

[18] H.D. Carlton, A. Haboub, G.F. Gallegos, D.Y. Parkinson, A.A. MacDowell, Damage evolution and failure mechanisms in additively manufactured stainless steel, Mater. Sci. Eng. A **651**, 406, (2016).

[19] G.T. Gray III, V. Livescu, P.A. Rigg, C.P. Trujillo, C.M. Cady, S.R. Chen, J.S. Carpenter, T.J. Lienert, S.J. Fensin, Structure/property (constitutive and spallation response) of additively manufactured 316L stainless steel, Acta Mater. **138**, 140, (2017).

[20] E. Zaretsky, A. Stern, and N. Frage, Dynamic response of AlSi10Mg alloy fabricated by selective laser melting, Materials Science and Engineering: A **688**, 364 (2017).

[21] G. Asala, J. Andersson, and O.A. Ojo, Improved dynamic impact behaviour of wire-arc additive manufactured ATI 718Plus® Materials Science and Engineering: A **738**, 111 (2018).

[22] M. Laurençon, T. de Rességuier, D. Loison, J. Baillargeat, J.N.D. Ngnekou, and Y. Nadot, Effects of additive manufacturing on the dynamic response of AlSi10Mg to laser shock loading, Materials Science and Engineering: A **748**, 407 (2019).

[23] G. Asala, J. Andersson, and O.A. Ojo, Analysis and constitutive modelling of high strain rate deformation behaviour of wire-arc additive-manufactured ATI 718Plus superalloy, Int J Adv Manuf Technol **103**, 1419 (2019).

[24] O. Klimova-Korsmik, G. Turichin, R. Mendagaliyev, S. Razorenov, G. Garkushin, A. Savinykh, R. Korsmik, High-strain deformation and spallation strength of 09CrNi2MoCu steel obtained by direct laser deposition, Metals **11**(8), 1305, (2021).

[25] A. Laurence, J. Cormier, P. Villechaise, T. Billot, J.-M. Franchet, F. Pettinari-Sturmel, M. Hantcherli, F. Mompiou, and A. Wessman, Impact of the solution cooling rate and of thermal aging on the creep properties of the new cast & wrought René 65 Ni-based superalloy, in *8th International Symposium on Superalloy 718 and Derivatives*, edited by E. Ott, A. Banik, J. Andersson, I. Dempster, T. Gabb, J. Groh, K. Heck, R. Helmink, X. Liu, and A. Wusatowska-Sarnek (John Wiley & Sons, Inc., Hoboken, NJ, USA, 2014), pp. 333–348.

[26] S. Gourdin, J. Cormier, G. Henaff, Y. Nadot, F. Hamon, and S. Pierret, Assessment of specific contribution of residual stress generated near surface anomalies in the high temperature fatigue life of a René 65 superalloy: Effect of surface anomalies on the fatigue life of a René 65 superalloy, Fatigue Fract Engng Mater Struct **40**, 69 (2017).

[27] S.E. Atabay, O. Sanchez-Mata, J.A. Muñiz-Lerma, and M. Brochu, Microstructure and mechanical properties of difficult to weld Rene 77 superalloy produced by laser powder bed fusion, Materials Science and Engineering: A **827**, 142053 (2021).

[28] S.E. Atabay, O. Sanchez-Mata, J.A. Muñiz-Lerma, R. Gauvin, and M. Brochu, Microstructure and mechanical properties of Rene 41 alloy manufactured by laser powder bed fusion, Materials Science and Engineering: A **773**, 138849 (2020).

[29] Q. Jia and D. Gu, Selective laser melting additive manufacturing of Inconel 718 superalloy parts: Densification, microstructure and properties, Journal of Alloys and Compounds **585**, 713 (2014).

[30] S.A. Sheffield and G.A. Fisk, Chapter VI: 7 - Particle velocity measurement in laser irradiated foils using orvis, in *Shock Waves in Condensed Matter 1983*, edited by J.R. ASAY, R.A. GRAHAM, and G.K. STRAUB (Elsevier, Amsterdam, 1984), pp. 243–246.

[31] S. Watson, M.J. Gifford, and J.E. Field, The initation of fine grain pentaerythritol tetranitrate by laser-driven flyer plates, Journal of Applied Physics **88**, 65 (2000).

[32] D.L. Paisley, R.H. Warnes, and R.A. Kopp, Laser-driven flat plate impacts to 100 GPa with sub-nanosecond pulse duration and resolution for material property studies, in *Shock Compression of Condensed Matter–1991*, edited by S.C. SCHMIDT, R.D. DICK, J.W. FORBES, and D.G. TASKER (Elsevier, Amsterdam, 1992), pp. 825–828.

[33] H. He, T. Sekine, and T. Kobayashi, Direct transformation of cubic diamond to hexagonal diamond, Appl. Phys. Lett. **81**, 610 (2002).

[34] M.W. Greenaway, W.G. Proud, J.E. Field, and S.G. Goveas, A laser-accelerated flyer system, International Journal of Impact Engineering **29**, 317 (2003).

[35] T. de Rességuier, H. He, and P. Berterretche, Use of laser-accelerated foils for impact study of dynamic material behaviour, International Journal of Impact Engineering **31**, 945 (2005).

[36] R. Fabbro, J. Fournier, P. Ballard, D. Devaux, and J. Virmont, Physical study of laser-produced plasma in confined geometry, Journal of Applied Physics **68**, 775 (1990).

[37] L. Berthe, R. Fabbro, P. Peyre, L. Tollier, and E. Bartnicki, Shock waves from a water-confined laser-generated plasma, Journal of Applied Physics **82**, 2826 (1997).

[38] L.M. Barker and R.E. Hollenbach, Laser interferometer for measuring high velocities of any reflecting surface, Journal of Applied Physics **43**, 4669 (1972).

[39] W.F. Hemsing, Velocity sensing interferometer (VISAR) modification, Review of Scientific Instruments **50**, 73 (1979).

[40]*LASL Shock Hugoniot Data*, Stanley P. Marsh (University of California Press, 1980).

[41] D.E. Grady, *The Spall Strength of Condensed Matter.* Journal of the Mechanics and Physics of Solids **36**, 353-384 (1988).

[42] T. Antoun, L. Seaman, D.R. Curran, G.I. Kanel, S.V. Razorenov, and A.V. Utkin, *Spall Fracture* (Springer, New York, 2003).

[43] G.I. Kanel, *Spall Fracture: Methodological Aspects, Mechanisms and Governing Factors* (2010).

[44] D.M. Shah and A. Cetel, Evaluation of PWA 1483 for large single crystal IGT blade applications, in *Superalloys 2000 (Ninth International Symposium)* (TMS, 2000), pp. 295–304.

[45] P. Fernandez-Zelaia, M.M. Kirka, A.M. Rossy, Y. Lee, and S.N. Dryepondt, Nickel-based superalloy single crystals fabricated via electron beam melting, Acta Materialia **216**, 117133 (2021).

[46] E. Balikci, R.A. Mirshams, and A. Raman, Tensile strengthening in the nickel-base superalloy IN738LC, Journal of Materials Engineering and Performance **9**, 324 (2000).

[47] J. Jiang, J. Yang, T. Zhang, J. Zou, Y. Wang, F.P.E. Dunne, and T.B. Britton, Microstructure sensitive crack nucleation around inclusions in powder metallurgy nickel-based superalloys, Acta Materialia **117**, 333 (2016).

[48] D. Texier, J. Cormier, P. Villechaise, J.-C. Stinville, C.J. Torbet, S. Pierret, and T.M. Pollock, Crack initiation sensitivity of wrought direct aged alloy 718 in the very high cycle fatigue regime: the role of non-metallic inclusions, Materials Science and Engineering: A **678**, 122 (2016).

[49] D. Texier, J.-C. Stinville, M.P. Echlin, S. Pierret, P. Villechaise, T.M. Pollock, and J. Cormier, Short crack propagation from cracked non-metallic inclusions in a Ni-based polycrystalline superalloy, Acta Materialia **165**, 241 (2019).

[50] D. Texier, A.C. Gómez, S. Pierret, J.-M. Franchet, T.M. Pollock, P. Villechaise, and J. Cormier, Microstructural features controlling the variability in low-cycle fatigue properties of alloy Inconel 718DA at intermediate temperature, Metall and Mat Trans A **47**, 1096 (2016).

[51] M.-A. Charpagne, P. Vennéguès, T. Billot, J.-M. Franchet, and N. Bozzolo, Evidence of multimicrometric coherent γ' precipitates in a hot-forged γ-γ' nickel-based superalloy, Journal of Microscopy **263**, 106 (2016).

[52] S. Katnagallu, S. Vernier, M.-A. Charpagne, B. Gault, N. Bozzolo, and P. Kontis, Nucleation mechanism of hetero-epitaxial recrystallization in wrought nickel-based superalloys, Scripta Materialia **191**, 7 (2021).

[53] M.-A. Charpagne, T. Billot, J.-M. Franchet, and N. Bozzolo, Heteroepitaxial recrystallization: A new mechanism discovered in a polycrystalline γ-γ' nickel based superalloy, Journal of Alloys and Compounds **688**, 685 (2016).

Table I. Nominal composition (in wt. pct) of the Rene 65 alloy

	Ni	Cr	Mo	W	Co	Fe	Nb	Ti	Al	Zr	B
Rene 65	Base	16	4	4	13	1	0.7	3.7	2.1	0.05	0.02

Table II. Comparison of the Hugoniot elastic limit, spall strength and strain rate between our average values and those reported for two other Ni-based superalloys[8]

	Rene 65 (this work)	Inconel 738 LC[8]	PWA 1483[8]
σ_{HEL}	~2.2 GPa	~1.7 GPa	~ 2.5 GPa
σ_{sp}	~5.2 GPa	~2.9 GPa	~3.6 GPa
$\dot{\varepsilon}$	~ 10^6 s^{-1}	~ 10^5 s^{-1}	~ 10^5 s^{-1}

Figure captions

Fig. 1. Inverse pole figure maps showing crystallographic orientations along the vertical direction (Z) in Rene 65 alloys prior to shock loading: cast and wrought (a), additively manufactured and subsolvus (b) or supersolvus (c) heat treated.

Fig. 2. Measured values of the density and sound velocities in the three materials under study.

Fig. 3. Schematic description of the setup used to characterize laser-driven acceleration of thin Al foils in water-confined geometry (a), and typical velocity profile recorded at the (bottom) free surface of such Al foil (b). The blue area is the distance traveled by the probed surface, equal to 250 µm after about 430 ns.

Fig. 4. Schematic description of the setup used to investigate the response of the Ni-based alloy to the impact of a laser-launched Al flyer. Lateral dimensions are reduced for readability (see text for details).

Fig. 5. Simple theoretical analysis in a pressure-particle velocity plot of the shocked and released states induced by the planar impact at 900 m/s (see Fig. 3b) of an Al flyer on a Ni-alloy target. Solid lines are the shock adiabats of Al (blue) and Ni-alloy (red), dashed lines are obtained by vertical symmetries. States 1, 2 and 3 are induced successively in the flyer and target materials (see text for details).

Fig. 6. Typical velocity profile recorded at the free surface (bottom surface in Fig. 4) of a cast and wrought Rene 65 superalloy impacted by a laser-launched Al flyer.

Fig. 7. Measured values of the yield strength (Hugoniot elastic limit) in the three types of tested specimens.

Fig. 8. Measured values of the spall strength in the three types of tested specimens.

Fig. 9. Sections extracted from a 3D reconstruction obtained by X-ray microtomography of a wrought Rene 65 sample impacted on its bottom surface. Three sections have been selected, from the periphery of the loaded zone (top) to its center (bottom), as schematically shown to the right.

Fig. 10. Overall optical (a) and high magnification SEM micrographs (b) and (c) of cross sections in a wrought Rene 65 specimen recovered after being impacted on its bottom surface by a 150 µm-thick Al flyer. Darker spots of ~3 µm-diameter are primary γ' precipitates, and white particles are carbides.

Fig. 11. Inverse pole figure map showing crystallographic orientations of a shock-recovered wrought Rene 65 target (a). The close view (b) corresponds to the zone inside the black rectangle. Orientations are given along the vertical direction, which is also the direction of shock application.

Fig. 12. SEM micrographs of a cross section in a subsolvus AM Rene 65 target impacted by a 150 µm-thick Al flyer on its bottom left surface (a). On the close-up view (b), dark spots of sub-µm size are secondary γ' precipitates. The yellow dashed line shows a grain boundary (clearly visible at lower magnification), where some voids have nucleated.

Fig. 13. SEM micrographs of the crater left in the free surface of a subsolvus AM Rene 65 target by the ejection of a spalled layer after impact of a 150 µm-thick Al flyer on the opposite surface (a). The close-up view (b) illustrates the presence of short cracks normal to the spall plane.

Fig. 14. Inverse pole figure maps showing crystallographic orientations in a shock-recovered subsolvus AM Rene 65 target: broad view of a crack (a) and detail (b) showing void nucleation at grain boundaries and crack propagation throughout a grain. Orientations are given along the vertical direction (Z).

Fig. 15. Inverse pole figure maps showing crystallographic orientations in a shock-recovered supersolvus AM Rene 65 sample: broad view (a) and detail (b) showing void nucleation at grain boundaries and a combination of transgranular and intergranular fracture. Orientations are along the vertical direction (Z).

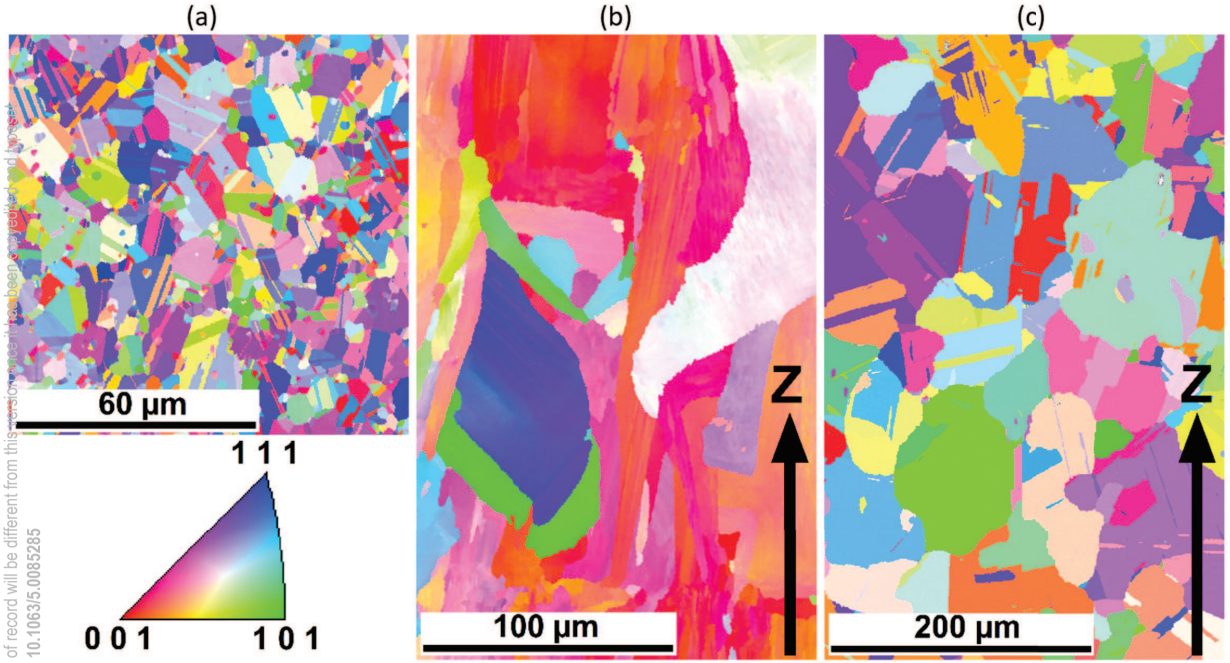

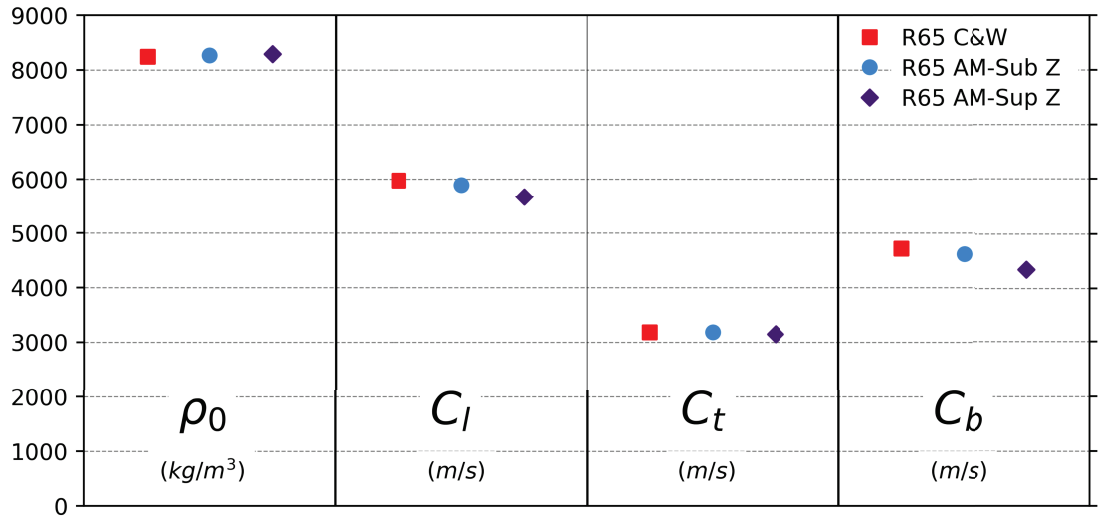

Journal of Applied Physics

(a)

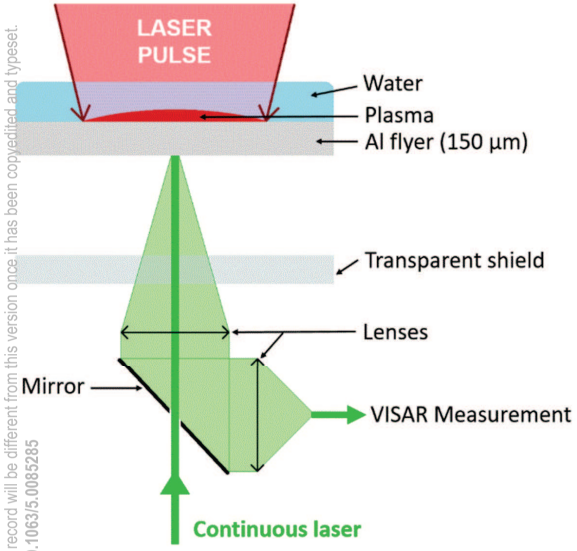

(b)

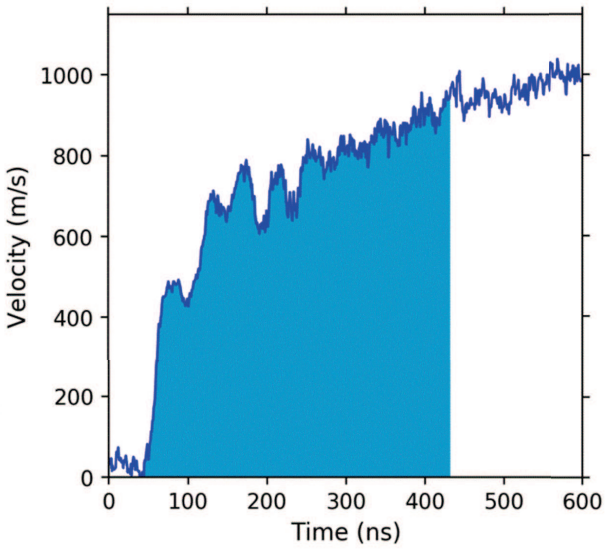

Journal of Applied Physics

PLEASE CITE THIS ARTICLE AS DOI: 10.1063/5.0085235

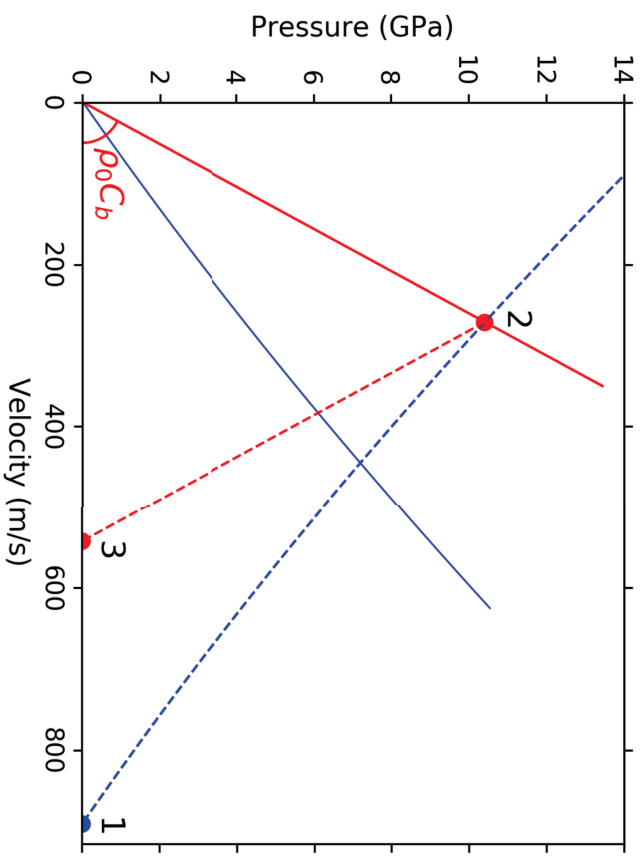

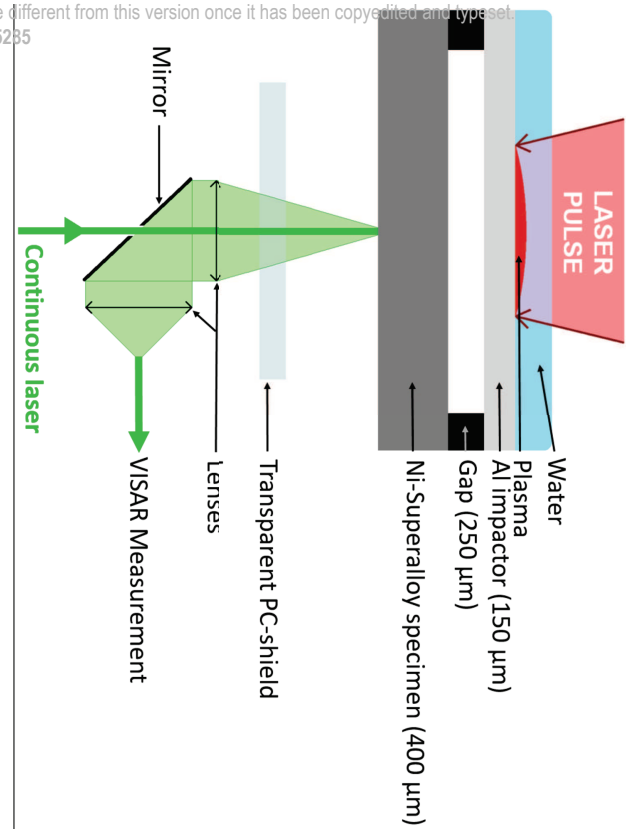

AIP Publishing

Journal of Applied Physics

ACCEPTED MANUSCRIPT

PLEASE CITE THIS ARTICLE AS DOI: 10.1063/5.0085285

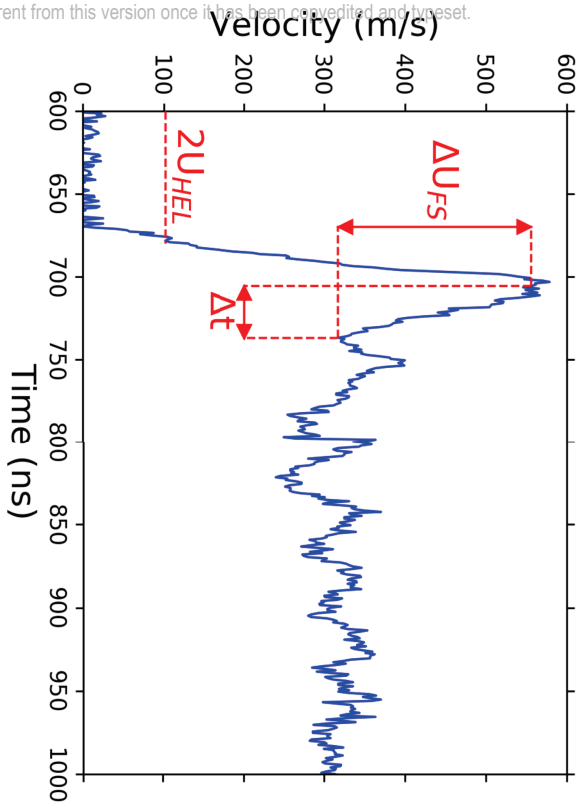

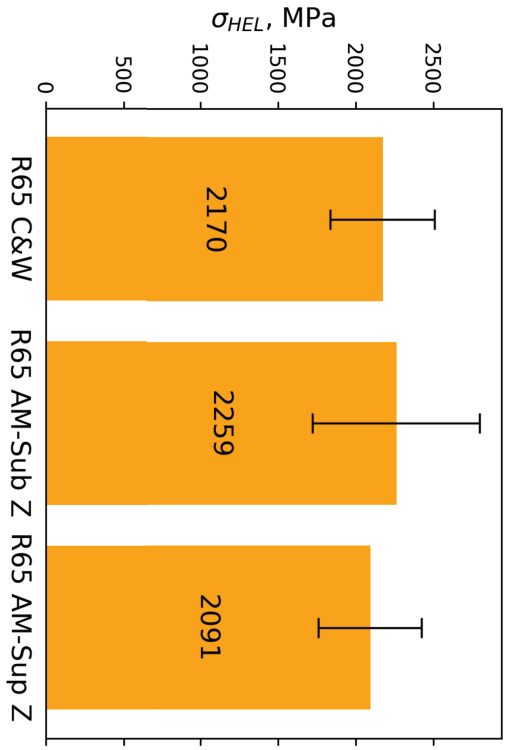

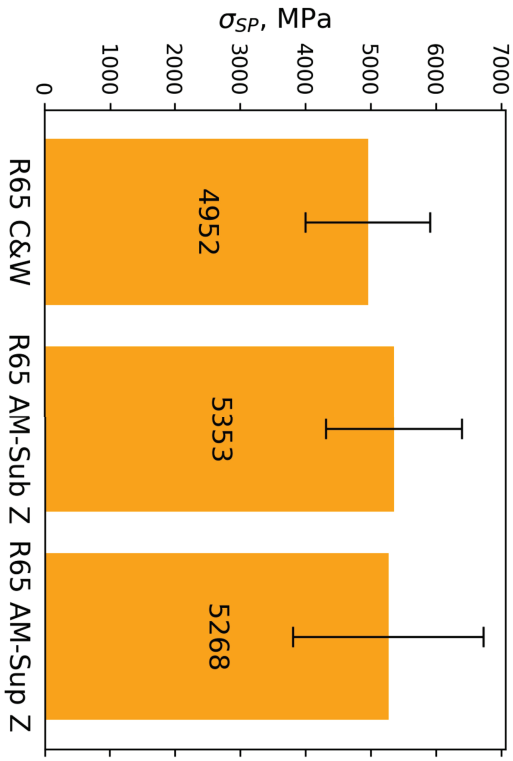

Journal of Applied Physics

PLEASE CITE THIS ARTICLE AS DOI: 10.1063/5.0085

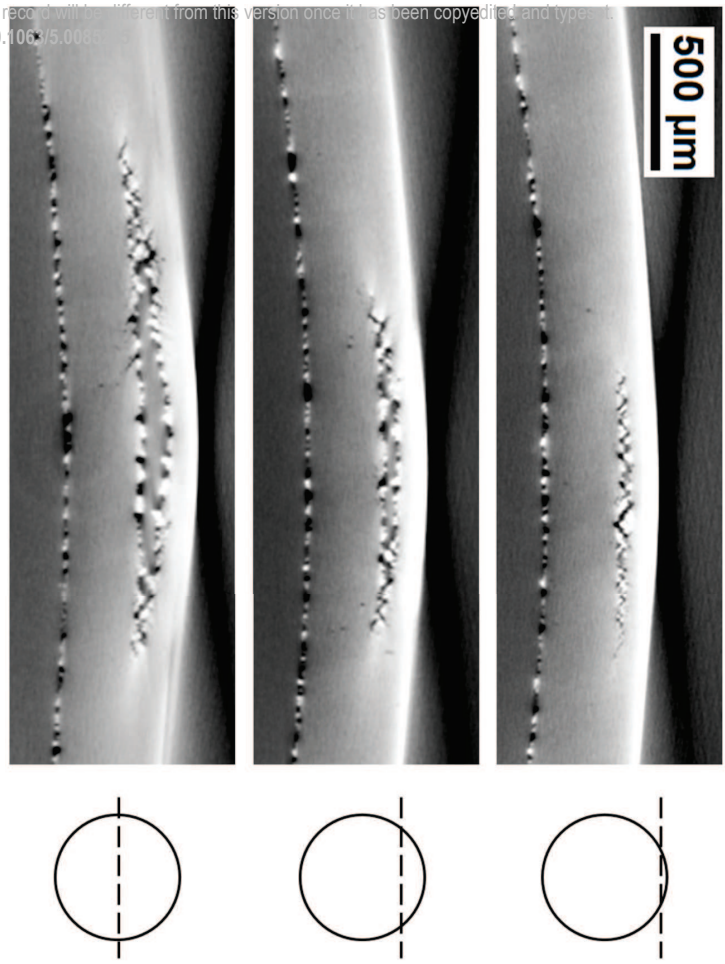

Journal of Applied Physics

ACCEPTED MANUSCRIPT

PLEASE CITE THIS ARTICLE AS DOI: 10.1063/5.0035185

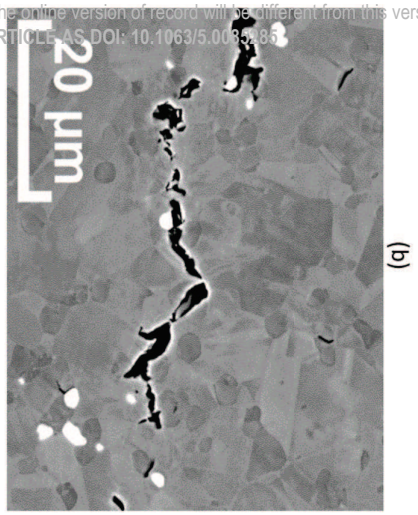

(b)

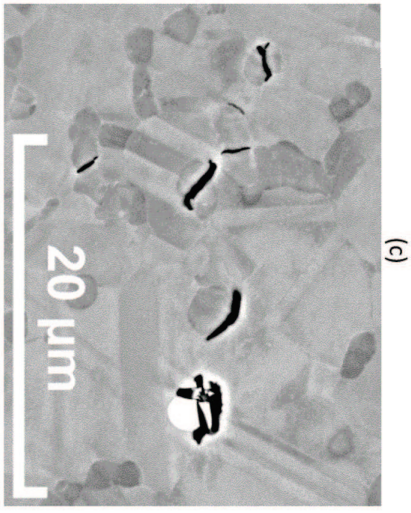

(c)

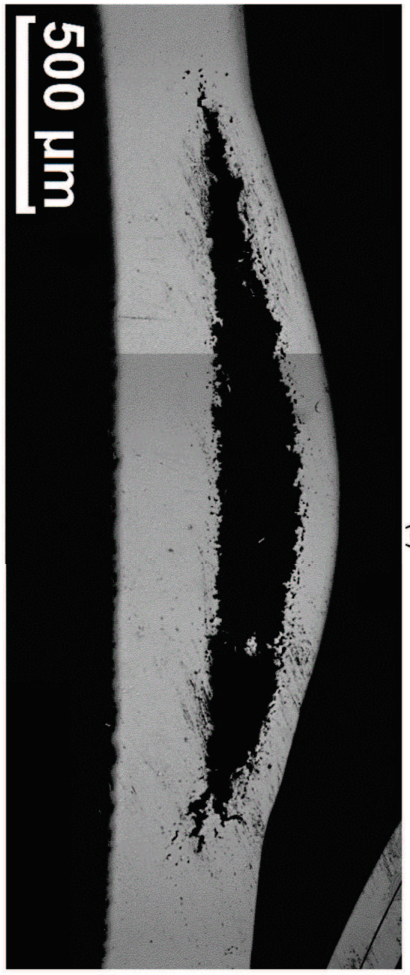

(a)

AIP Publishing
Journal of Applied Physics
ACCEPTED MANUSCRIPT

PLEASE CITE THIS ARTICLE AS DOI: 10.1063/5.0083285

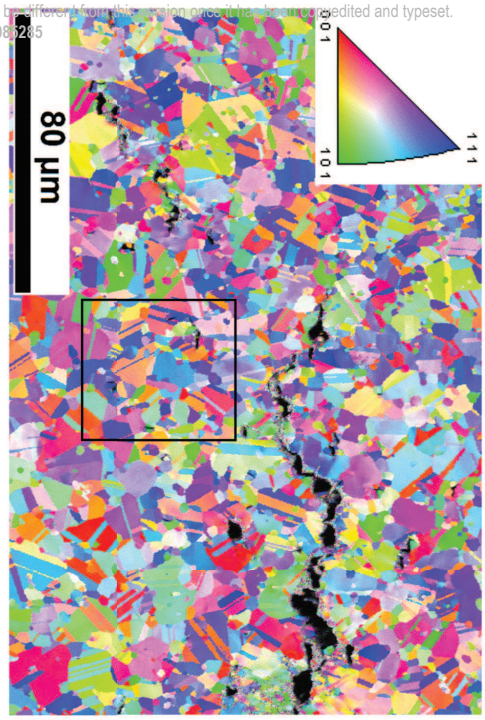

(a)

(b)

AIP Publishing
Journal of Applied Physics
ACCEPTED MANUSCRIPT

PLEASE CITE THIS ARTICLE AS DOI: 10.1063/5.0088785

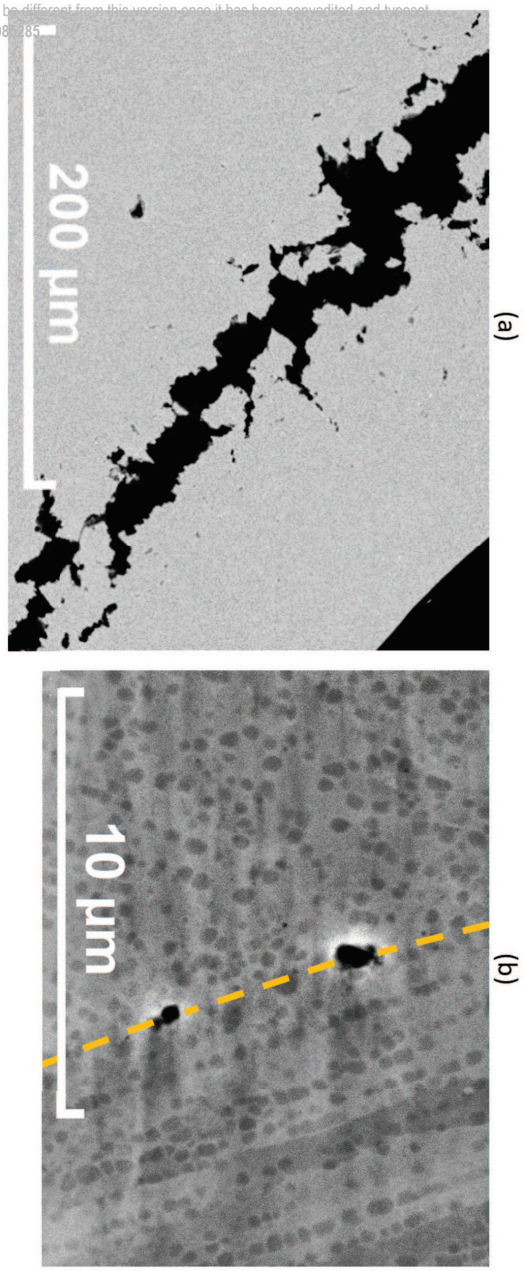

AIP Publishing
Journal of Applied Physics
ACCEPTED MANUSCRIPT

PLEASE CITE THIS ARTICLE AS DOI: 10.1063/5.0085285

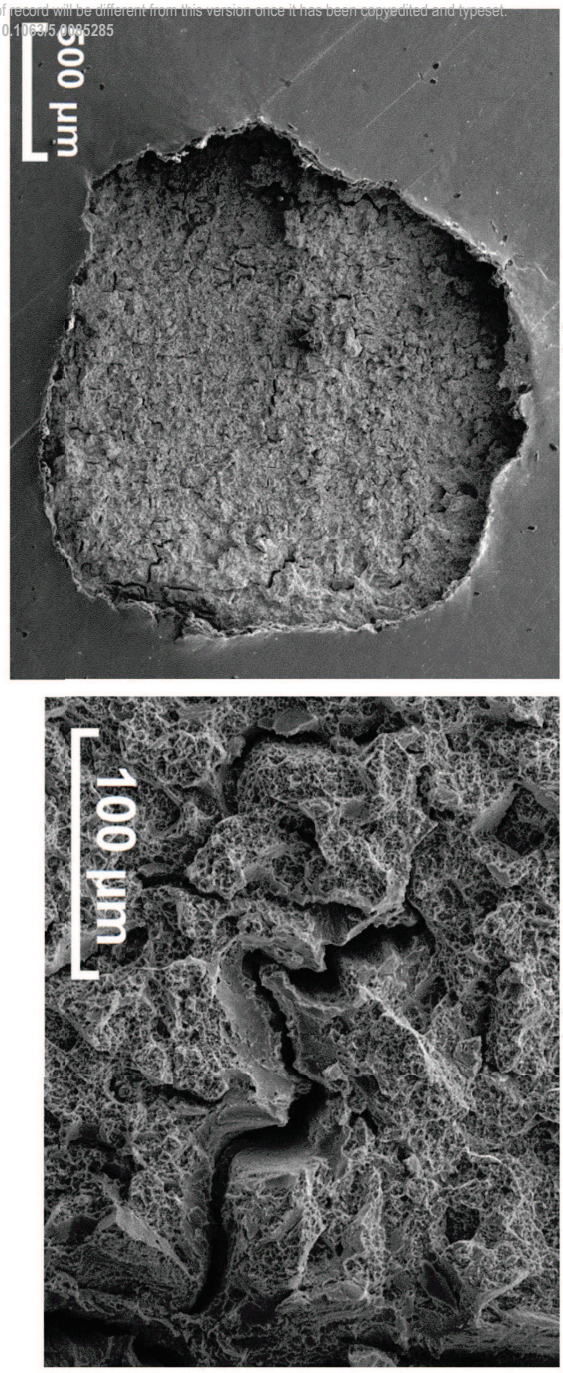

AIP Publishing
Journal of Applied Physics
ACCEPTED MANUSCRIPT

PLEASE CITE THIS ARTICLE AS DOI: 10.1063/5.0085285

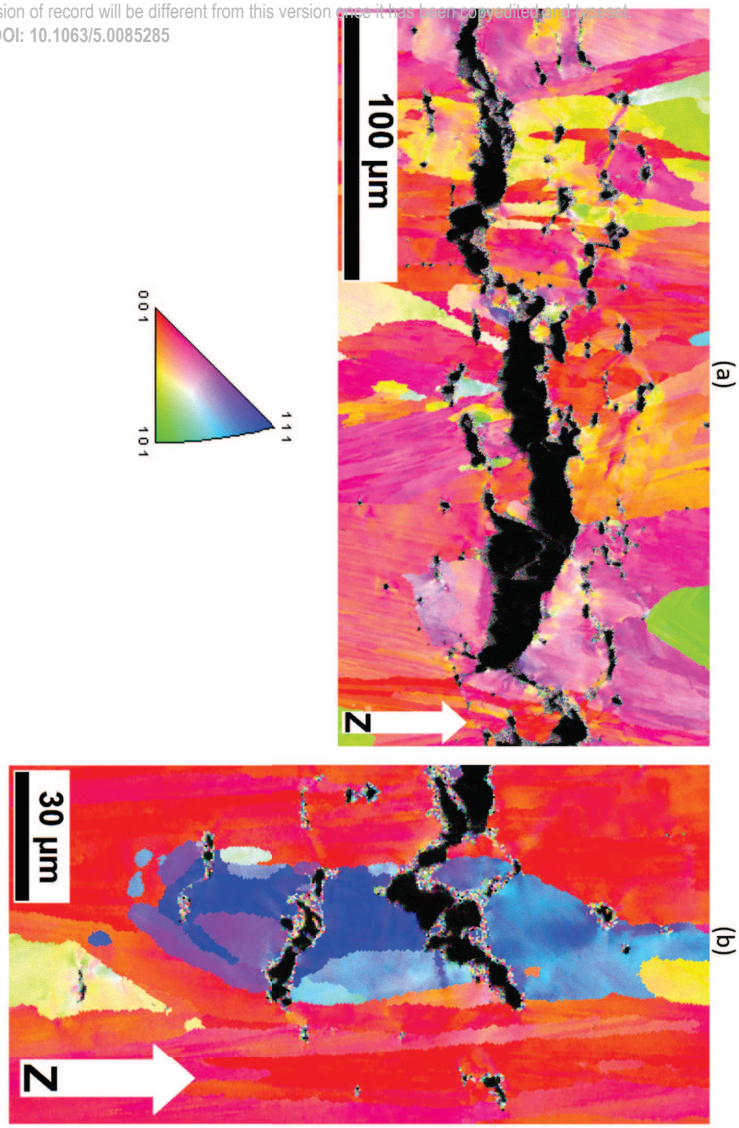

Journal of Applied Physics

PLEASE CITE THIS ARTICLE AS DOI: 10.1063/5.0085285